Pulsed-injection metal organic chemical vapour deposition for the development of copper silicate and silicide nanostructures

Richard. O'Donoghue[1], Arunas Teiskersis[1], Yurii K. Gun'ko[1, 2*]

[1]*School of Chemistry and CRANN Institute, Trinity College Dublin, Dublin 2, Ireland.*
[2]*ITMO University, 197101, St. Petersburg, Russia*

[*]Corresponding author, E-mail: igounko@tcd.ie

Received: 25 October 2016, Revised: 12 February 2017 and Accepted: 07 April 2017

DOI: 10.5185/amlett.2017.1465
www.vbripress.com/aml

Abstract

In this manuscript we report the production of copper silicate and silicide nanostructures: octahedral o-Cu(SiO_3), wire w-Cu(SiO_3) and wire w-Cu_3Si (embedded in silicate shell) using copper bis(2,2,6,6-tetramethyl-3,5-heptanedionate) [Cu(tmhd)$_2$] precursor and the pulsed injection metal organic chemical vapour deposition (PI-MOCVD) technique. In our experiments, particular attention has been paid to the structural composition and morphological analysis of the nanostructures which are dictated by the deposition parameters such as deposition temperature, carrier gas flow rate and injection time. Deposition processes were diffusion limited and various methods were used to show that by changing the amount of stress relaxation via the reaction time, concentration and flow rate, w-Cu(SiO_3) and w-Cu_3Si could be made to evolve. Nanostructures have been characterised by x-ray diffraction (XRD), Raman, scanning tunneling electron microscopy (STEM) and atomic force microscopy (AFM) techniques. It was found that the presence of oxygen (SiO_2) in the silicon substrates and exposure of the nanostructures to ambient conditions results in the formation of copper silicate from initially produced copper silicide nanomaterials. This work outlines the potential for the manufacturing of various patterned copper nanostructures via PI-MOCVD. Copyright © 2017 VBRI Press.

Keywords: MOCVD, copper silicide, copper silicate, nanostructures, nanowires.

Introduction

Metal silicides represent a wide set of refractory materials that are currently in use in CMOS devices, bulk structural components, thermoelectrics, photovoltaics and thin film coatings [**1**]. Many of these applications may be improved by their conversion into one-dimensional nanomaterials. Copper silicides have been envisaged as very promising interconnect materials due to their unique properties and ubiquity of Cu within microelectronics processing. Also there is a potential for Cu diffusion suppression via the usage of Cu silicides when compared with the pure metal [**2**]. In particular, copper silicide based thin films have found use as ion diffusion barriers and as passivation layers for on chip applications [**3**].

Copper silicide formation in the bulk has been studied by many research groups over the past forty years [4–8]. It was discovered that after a slow cooling process, samples with a very large concentration (~10^{17} cm^{-1}) of copper formed precipitate colonies mainly, in the near surface region of the wafer. The growth of these precipitate colonies was explained by the nucleation of new copper precipitates on stacking faults and dislocation loops that had already been punched out by the existing precipitates [**9**, **10**]. Istratov *et al.* in contrast to this, illustrated that a sample when rapidly quenched to room temperature formed small platelet like precipitates approximately 30-200 nm in diameter with a density of up to 10^{-13} cm^{-1}, spread homogeneously throughout the bulk of the sample [**11**]. The outstanding feature of the precipitation behavior of Cu in Si to form copper silicide is the associated expansion of the lattice. The main phase of copper silicide at room temperature, namely η-Cu_3Si [**12**], has a large molecular volume around 46Å in comparison to the 20Å of regular silicon [**13**]. Therefore, this means that around 1.3 Si interstitial atoms are ejected for each Si atom to create a Cu_3Si precipitate and that growth and nucleation requires a higher driving force for precipitation than most other metals. Though the amount of energy required varies depending upon the Si crystalline quality, as obviously homogeneous nucleation for when a precipitate has to be created in a perfect lattice will have a higher barrier than heterogeneous nucleation for when precipitates nucleate at already existing defects like vacancy clusters. Thus it is very likely that Cu will fill lattice defects whenever they are present [**14**]. Though it has been shown before that Cu does not decorate all types of defects but instead prefers, Frank type partial dislocations [**15**], grain boundaries [**16**] and stacking faults [**17**,**18**]. Cu_3Si is the predominant phase that is reported in the literature for copper silicides in

nanocrystal morphologies with nanosquares, nanoplatelets, nanotriangles and nanowires being created via the deposition of copper from various sources onto a silicon substrate. This can be carried out by using a whole host of different methodologies as illustrated in **Table 1**. Pulsed injection MOCVD differs from traditional chemical vapour deposition techniques in that the liquid or a solid (provided it has been dissolved by an appropriate solvent) precursor is kept at room temperature and the small droplets produced are subsequently pulsed into the evaporation chamber via an electromagnetic valve. The process allows a precursor to be injected in short and sharp pulses into the reaction chamber of the MOCVD reactor directly, via a spray nozzle injector or vaporizer which provides additional benefits to the process such as fast growth rates, low contamination, and low cost [**19**]. It can also allow for greater control over the amount of precursor used, its flux and the concentration. To date the growth of Cu_3Si nanostructures has never been attempted using the aforementioned technique. However, the precursor copper bis(2,2,6,6-tetramethyl-3,5-heptanedionate) [$Cu(tmhd)_2$], has been used previously in combination with PI-MOCVD in order to grow mixed films of $CaCu_2O_x$ with [$Ca(tmhd)_2$] [**20**] and also CuCrO with [$Cr(tmhd)_2$] [**21**] both for TCO applications.

In this paper, we report the first preparation of copper silicide and silicate nanostructures grown on silicon (100) by PI-MOCVD using the metalorganic [$Cu(tmhd)_2$] precursor and the solvent 1,2-dimethoxyethane. Particular attention has been paid to the structural composition and morphological analysis of the nanostructures which are dictated by the deposition parameters of the PI-MOCVD process such as, deposition temperature, carrier gas flow rate and injection time. This work particularly highlights the kinetic and thermodynamic interplay in the formation of the nanostructures as it is shown how w-Cu_3Si could be made to evolve through the resultant stress relaxation upon the silicon lattice using the prementioned parameters. This research puts foreward a potential for the fabrication of various patterned copper nanostructures using PI-MOCVD.

Experimental

Materials/ chemicals details

Table 1. Different research methodologies for the fabrication of various copper nanostructures.

Method	Copper Source	Reaction Temperature (°C)	Self-Assembled Nanostructures	Year	Ref
PI-MOCVD	$Cu(tmhd)_2$	600-900	Octahedral $Cu(SiO_3)$ Platelet & Wire $Cu(SiO_3)$ Cu_3Si-Nanowires (in a silicate shell)	2016	Current Work
Pulsed laser deposition	Metallic Copper Target	20-700	Cu_xSi_{1-x} Nanoplatelets Cu_xSi_{1-x} Nanotriangles Cu_xSi_{1-x} Thin films	2016	Zhang *et al.*[**24**]
Magnetron Sputtering & Annealing (& Focused Ion Beam lithography)	Cu/Ge Bilayer	650	Free Standing Single crystal Cu_3Si Nanowires (& position controlled Single crystal Cu_3Si)	2015 2012	Jung *et al*. [**25,26**]
Molecular Beam Epitaxy	Cu from an Effusion Cell	550	Cu_3Si Nanotriangles Cu_3Si Nanoislands Cu_3Si Nanowires (Co coated)	2014	Ermakov *et al.* [**27**]
Semi batch reaction	Cu Substrates	420-475	Cu_3Si Nanowires	2013	Yuan *et al.*[**28**]
Electron Beam Evaporation	Cu Pellets	600	Cu_3Si Nanowires	2012	Ng *et al*.[**2**]
Electron Beam Lithography & Vapour Transport & Vapor-Liquid-Solid (VLS) Mechanism (Gold Thin Film)	Cu Pads	350	Cu_3Si/Si Nanowire Heterostructures	2013	Chiu *et al*.[**29**]
High Boiling Point Solvent System	Cu Foil	460	High density arrays of $Cu_{15}Si_4$ Nanowires	2012	Geaney *et al*.[**30**]
Chemical Vapour Deposition (CVD)	Cu-coated Si substrate	470-550	Cu_3Si/Si Nanowires	2010	Wen *et al.*[**31**]
Vapour Transport	Cu & CuO Powder	650-900	Octahedral shaped Cu_3Si Spindle shaped Cu_3Si Wire shaped Cu_3Si	2010	Li *et al.*[**32**]
Vapour Transport VLS Mechanism (30nm Gold Colloids)	Cu Powder	1050	Crystallite Cu_3Si/ Si Nanowires	2010	Johnson *et al.*[**33**]
Vapour Transport (Gold nanoparticles)	CuO Powder	900	Cu_3Si Nanosquares Cu_3Si Nanotriangles Cu_3Si Nanowires	2008	Zhang *et al.*[**34**]
Laser Ablation	Mixed Cu/Si Powders (& Ball Milling)	1200	Nanocomposite Cu_3Si crystallites in Si Nanowires	2000	Qi *et al*.[**35**]

All chemicals were purchased from Sigma-Aldrich unless stated otherwise.

Material synthesis / reactions

Copper bis(2,2,6,6-tetramethyl-3,5-heptanedionate) was prepared according to the standard method described by Hammond *et al.* [**22**]. The FTIR spectrum of the precursor illustrated bands and peaks equivalent to those already reported [**23**]. The thermal behaviour of the compound was investigated by thermogravimetric analysis (TGA) under a flow of inert nitrogen (20 ml/min) and revealed that under experimental conditions, $Cu(tmhd)_2$ began evaporating at 116 °C until it fully decomposed at 213 °C to give nil residue. The weight loss occurs essentially in a single step due to sublimation of the solid. A T_{50} value of 203°C highlights that the precursor is stable up to relatively high vaporization temperatures which indicates substantial vapour-phase stability and markedly clean transport properties. These characteristics allow the precursor to travel to the heated substrate in the MOCVD chamber and react before it decomposes.

Nanostructure deposition

$Cu(SiO_3)$ nanostructures were grown by a PI-MOCVD technique on monocrystalline silicon (100) substrates. The samples were cut into 1 cm x 1 cm from silicon (100) wafers and adhered to a removable holder using conductive silver ink (Alfa Aesar) and heat. The metallic holder was secured vertically into the reactor, essentially parallel to the oncoming gas flow direction. The Si samples were cleaned with a successive acetone and isopropyl alcohol wash prior to loading into the deposition chamber. The $Cu(tmhd)_2$ was dissolved in the very volatile solvent anhydrous 1,2-dimethoxyethane (0.025M) and an amount n were injected into the evaporation chamber in a very controlled manner via an electromagnetic actuated valve in 2.2 ms long pulses, every half of a second where it was flash evaporated in the evaporation zone which was held at 150-160°C and carried to the deposition chamber via a controlled flow of Argon (between 50/50-400/400 ml/min). The droplets averaged ~6 mg in mass and the deposition temperature ranged from 600-900 °C. A pressure of ~0 torr was maintained during initial heating and ~5 torr was upheld in the vacuum system during the deposition. The furnace was heated up and cooled down naturally and held at the desired temperature until the deposition was complete. Depositions were performed under different conditions in order to optimize nanostructure growth. For the growth of $Cu(SiO_3)$ nanostructures on Si (100) substrates, a design of experiment-like approach was taken. The carrier gas flow rate was varied between 50/50 ml/min and then incrementally doubled up to 400/400 ml/min whilst keeping all other parameters constant The substrate temperature was increased in 50 °C increments from 600 to 900°C. All deposition temperatures shown were held at 700°C unless stated otherwise. The evaporation temperature was held at 90, 120 and 150 °C. The injector time began at 0.5 s and was then systematically doubled up to a 2 s interval for injection. After depositions, the nanostructures were cooled to room temperature either naturally in vacuum or in an argon pressure of 1 torr.

Characterisations / device fabrications /response measurements

Thermogravimetric analysis of the precursor was performed using a Perkin Elmer Pyris 1 TGA thermogravimetric analyser in the range 30-350℃ at ambient pressure using ~5 mg of sample, at a heating rate of 5℃ min^{-1} in a ceramic crucible using an N_2 flow rate = 20 ml/min. Fourier Transform Infrared (FTIR) spectra were recorded on a Perkin-Elmer spectrum 100 FTIR/ATR spectrometer at room temperature. FTIR spectra were collected over a range of 4000-650 cm^{-1} by averaging 64 scans collected at a resolution of 4 cm^{-1}. The morphologies of the nanostructures were analysed by a Tescan Mira XMU Variable Pressure Field Emission Scanning Electron Microscope in the Centre for Microscopy Analysis (CMA) and a Carl Zeiss Ultra SEM in the Advanced Microscopy Lab (AML). Samples were prepared for transmission electron microscopy (TEM) using a Carl Zeiss Auriga Focused Ion Beam (FIB) system where a thin layer of Pt was deposited upon an area of interest on the samples to protect their subsurface morphologies. The samples were cut and milled with an acceleration voltage of 30keV until a lamella of ~100 nm was formed. This was then transferred onto a copper grid where it was further milled with a lower acceleration voltage of 5keV in order to polish it. A FEI Titan transmission electron microscope was used to characterise the lamella, with an accelerating voltage of 300keV, by using scanning transmission electron microscopy (STEM) and energy dispersive analysis of X-Rays (EDX). XRD patterns were recorded using a Siemens D500 diffractometer. The samples were exposed to the Cu Kα radiation (λ =1.54 Å) at room temperature in the range 15-65º (2θ). AFM analysis using an Asylum MFP –3D stand-alone atomic force. Raman spectra were recorded using a Renishaw 1000 Micro-Raman system equipped with an Ar+ ion laser (Laser Physics Reliant 150 Select Multi-Line) which had an excitation wavelength of 514.5 nm and a typical 3 mW laser power used at 10%.

Results and discussion

Deposition of copper silicates and silicides on Si(100) substrate

Depositions were carried out using different parameters in order to optimise nanostructure growth. Several of these experimental parameters were varied such as, deposition temperature (T_{dep}), carrier gas flow rate & composition and injection time. For the growth of $Cu(SiO_3)$ nanostructures on Si (100) substrates, the previously mentioned design of experiment-like approach was taken whereby a series of experiments were designed over a range of parameters. Then by alternating an individual parameter whist keeping the others constant, an outcome or influence can be determined upon the overall system. $Cu(tmhd)_2$ was used as a precursor in all experiments and general conditions for deposition are presented in **Table 2**. To investigate the growth of $Cu(SiO_3)$ based nanostructures, an optimal

deposition temperature was initially determined. This was achieved by carrying out several depositions at both low concentrations (n=50) and flow rates (50/50 ml/min) over a wide temperature range from 600 °C to 900 °C with the deposition temperature being increased systematically in 50 °C intervals with each experiment. The deposited samples have been initially investigated by SEM to ensure the formation of nanostructures of defined morphology. The samples were also investigated by XRD and selected optimised samples have been studied by Raman spectroscopy, STEM and AFM analysis, in order to study the structure and nature of these nanomaterials.

Table 2. Deposition conditions for $Cu(SiO_3)$ nanostructures and Cu_3Si nanowires.

Deposition Temperature	600-900 ºC
Evaporation Temperature	90-160 ºC
Carrier Gas Flow (Ar + O_2)	100-800 ml/min
Reactor Pressure	5 torr
Metalorganic Precursor	$Cu(tmhd)_2$
Solvent	1,2- dimethoxyethane
Molarity	0.025 mol/l
Concentration (No. of droplets - n)	50 – 200
Impulse Frequency	2.2 Hz
Microdose Mass	~6 mg
Injection Time	0.5 – 2 seconds

X-ray diffraction analysis

XRD studies of all deposited samples illustrated the same diffraction pattern. The typical XRD pattern of the samples deposited at 700 °C are shown in **Fig. S1** and **S2** (see supporting information). XRD data from the JCPDS was used to allocate the reflections to the individual crystallographic orientation of all phases present. From examining the diffractogram, it can be seen that the nanostructures are a combination of two different types of copper silicate. There are three peaks in the pattern. The most intense peak at 2θ = 38.70° with a d spacing of 2.327 corresponds to the orthorhombic (111) of copper polysilicate (2θ = 38.60°, JCPDS pattern no: 01-070-3326) which is the primary phase observed in the sample. A FWHM value for this reflection of 0.54 indicates that these silicate structures are highly crystalline. The smallest and medium reflections at 2θ = 30.30° and 33.90° with d-spacings of 2.647 and 2.946 were assigned to the (401) and (321) rhombohedral crystallographic orientation of copper silicate respectively (2θ = 30.85°, 34.70°, JCPDS pattern no: 00-032-0346). The FWHM values of 0.56 and 0.22 indicate that these silicate structures are highly crystalline, more so in the case of the (321) $CuSiO_3$ phase than that of the (401) phase which is slightly more amorphous. The high and narrow shape of the peaks illustrates that the individual crystallite domains are relatively periodic and in phase. An average crystallite size (D) of the nanostructures was calculated from the FWHM of the $Cu(SiO_3)$ (111) reflection using Scherrer's formula. The bulk value for this 2θ angle is 38.67° with a FWHM of 0.55 which yields an average crystallite value of 3.23 nm for the structures grown at 700 °C. There was a slight increase in D for those grown at 900 °C to 3.307 nm. A Fourier ptychographic microscopic (FPM) evaluation of this pattern was run by comparing it against a model obtained from the National Institute of Standard and Technology (NIST) which found

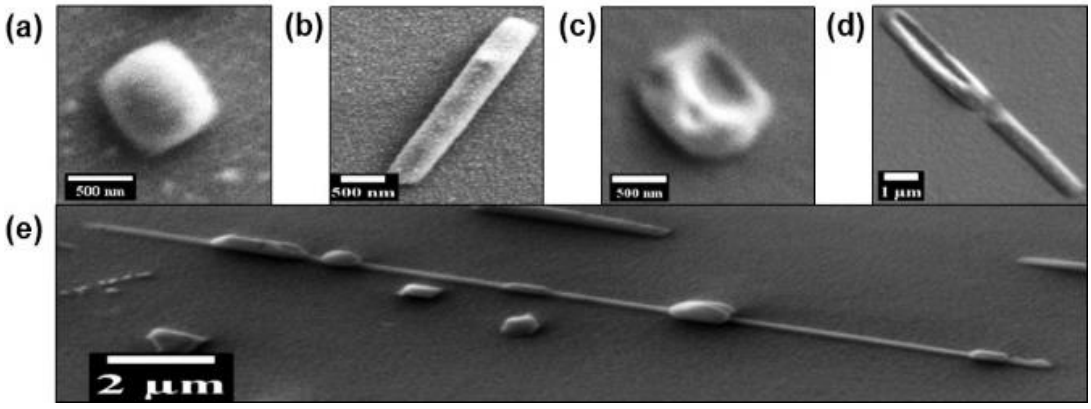

Fig. 1. SEM images of typical features grown upon Si(100). (a) o-$Cu(SiO_3)$ at 750 °C, (b) w-$Cu(SiO_3)$ at 750 °C, (c) o-$Cu(SiO_3)$ at 900 °C, (d) w-$Cu(SiO_3)$ at 900 °C and (e) elongated w-$Cu(SiO_3)$ at 750 °C.

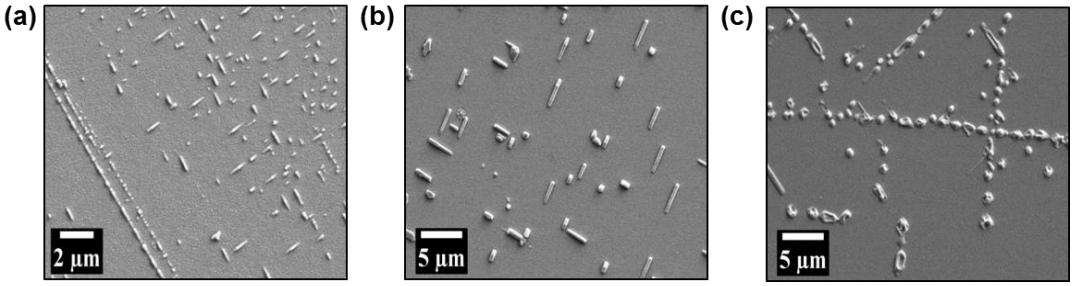

Fig. 2. SEM images of the o-$Cu(SiO_3)$ and w-$Cu(SiO_3)$ nanostructures grown upon Si(100). Samples above were grown at a flow rate of 50/50 ml/min with a concentration of n=50 and a deposition temperature of (a) 600 °C, (b) 750 °C & (c) 900 °C.

the silicate peaks had an overall compositional ratio of 57% CuO and 43% SiO_2.

Optimisation and SEM analysis of deposited nanostructures

Initial SEM images showed the formation of a series of $Cu(SiO_3)$ nanostructures such as the rounded nanosquares that are almost octahedral in shape and the platelet structures (see **Fig. 1**).

The rounded nanosquares correspond to o-$Cu(SiO_3)$ phase and range from 0.5-1 μm in dimensions, while the rod-like w-$Cu(SiO_3)$ can range anywhere from 0.5–2.5 μm in length and from 50-500 nm in diameter. Depending on the temperature range, the nanostructures were of two varieties. Lower temperature (600-750 °C) depositions resulted in the formation of more intact and defined configurations of the shapes described above within an overall rounded surfacial framework.

longer cleaner sub-surface w-$Cu(SiO_3)$ with lengths around 10 μm were observed for a flow of 50/50 ml/min and up to 16 μm for a rate of 100/100 ml/min and concentration of n=100. The structures were interspersed with various other features which also grew during the deposition such as o-$Cu(SiO_3)$ and surface w-$Cu(SiO_3)$ nanostructures. Average diameters were 225 nm and 380 nm for both the lower flow rates of 50/50 ml/min and 100/100 ml/min respectively.

It was also noted that for the 200/200 ml/min rates, condensed clusters of surface w-$Cu(SiO_3)$ platelets dominated the morphology. This behaviour was also recognised in the sample deposited at 400/400 ml/min rate (**Fig. 4**). This demonstrates that kinetic and thermodynamic factors influence the nanowire formation together with the concentration and the carrier gas flow rate which is sensitive to an increased rate of flux. Taking this into account, the injection time between each pulse time was elongated from 0.5–1 second and then finally up to 2

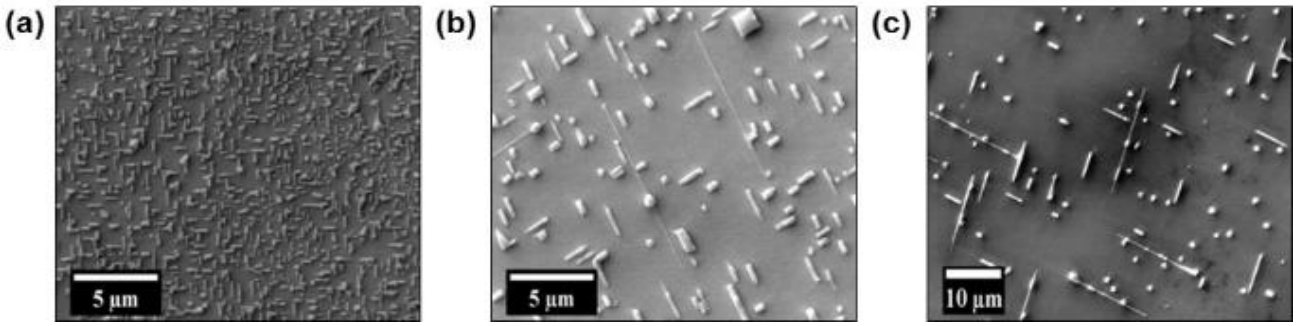

Fig. 3. SEM images of the growth of nanowires. Samples above were grown at n=100 and (a) 50/50 ml, (b) 100/100 ml & (c) 200/200.

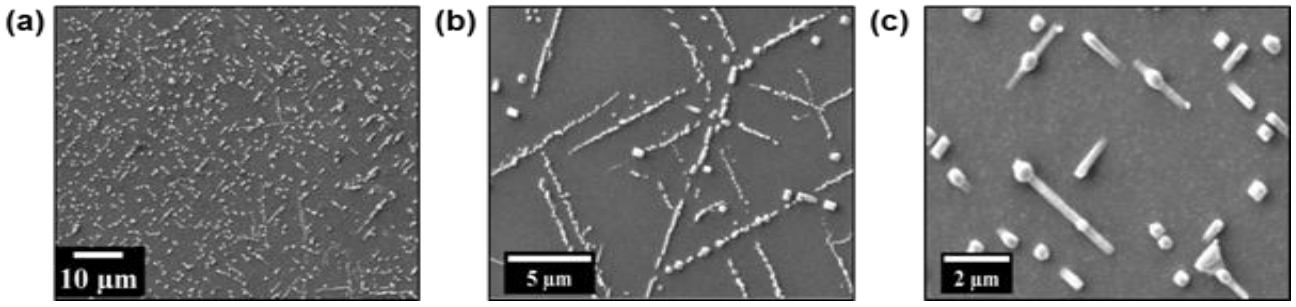

Fig. 4. SEM images of the growth of surface o-$Cu(SiO_3)$ and w-$Cu(SiO_3)$ at 400/400 ml/min at different magnifications.

Higher deposition temperatures (800-900 °C) yielded irregularly patterned arrangements with a more truncated structure as can be seen in **Fig. 2.** A series of experiments alternating the concentration of the Cu precursor and the gas flow rate was then performed. The number of injections of precursor material was varied in succession, at either n=50 or n=100, across a range of flow rates, from 50/50 ml/min-400/400 ml/min in order to analyse the effect of the carrier gas flow rate upon product morphologies. These structures are the result of nucleation at point defects inherent in the silicon (see **Fig. S3** in supporting information). The structures eventually transform into more platelet and spindle- shaped w-$Cu(SiO_3)$, depending on the rate of flux of the material. With an increased rate of flow, lengths up to 5 μm were reached while diameters grew to an average of 200 nm. It was found that enhanced nanowire growth came as a result of an increase in the concentration at these flow rates (**Fig. 3**). An abundance of seconds while the other parameters remained fixed. The carrier gas flow rate was set to 50/50 ml/min while the concentration was held at n=50. The SEM results are shown in the **Fig. 5** below. There is a clear evolution in the length of the wires as the time increases from on average 1.36 μm with a mean width of 272 nm, for the fastest injection time, to 4.27 μm with diameters of 328 nm, for the one second injection rate and to 6.26 μm and 314 nm for the slowest injection interval of 2 seconds. This shows that there is an almost linear progression between the lengths of the nanowires and the flux of the material. The evaporation temperature did not affect the growth of the nanostructures. This is most likely due to $Cu(tmhd)_2$ being highly volatile and thermally stable within the evaporation temperature range. This precursor sublimes at low temperature under vacuum (~100 °C) [**36**] and all temperatures used (90 °C , 120 °C, 150 °C) fall within its sublimation temperature window.

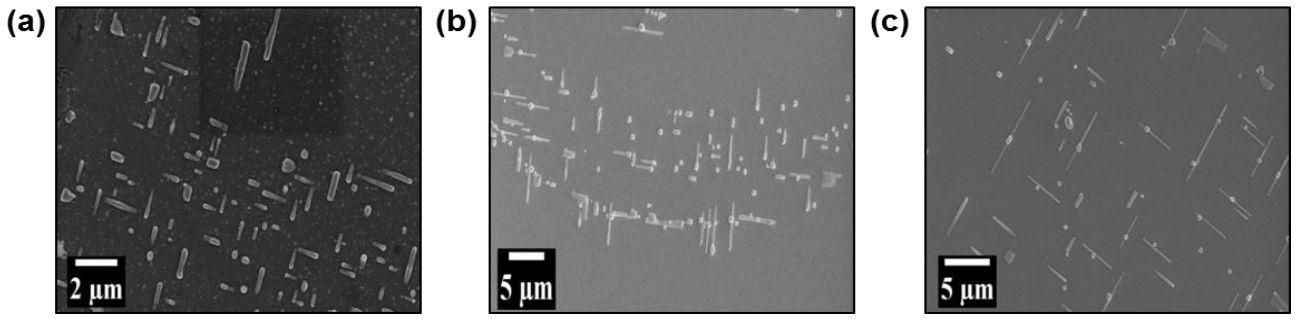

Fig. 4. SEM images of samples grown at varying injection times (a) 0.5 s, (b) 1 s & (c) 2 s. There is a visible connection between the lengths of the structures and the rate of flux.

AFM analysis

AFM analysis was carried out for a range of different concentrations and these data were used to define the optimal conditions for Cu(SiO_3) nanowire growth. This was done by varying the no. of droplets from 100–1000 in increments of 200. Analysis of the optimum conditions depicted that the growth of the best quality Cu(SiO_3) nanostructures occurred when both the concentration (n) and the rate of flow parameters were relatively low i.e. when the number of pulses was 50 and the rate of argon flow was kept at either 50/50 or 100/100 ml/min, keeping in accordance with the SEM analysis. It also highlighted the fact, much like the SEM results, that the Cu(SiO_3) forms early during the deposition process as long continuous and relatively clean nanowires which appear embedded within the substrate (**Fig. S4**, supporting information). According to AFMs, the w-Cu(SiO_3) grown were between 200-400 nm in diameter, up to 10 µm in length and have a relatively high aspect ratio. As the sample was relatively rough, it was therefore harder to image. The white blotches that appear in the images are a mixture of o-Cu(SiO_3) and w-Cu(SiO_3) that appear upon the surface of the substrate.

Raman spectroscopy of deposited nanostructures

Raman analysis was carried out on selected samples and it was almost complimentary to the characterisation by XRD and STEM studies by illustrating that the major components consisted of copper-silicate. Raman spectra of deposited samples were compared to the vibrational spectra of copper polysilicate (Cu(SiO_3)) previously published by Meibohm *et al.* [**37**] which obtained copper polysilicate by the thermal decomposition of dioptase ($Cu_6Si_6O_{18}.6H_2O$) and assigned observed modes based upon single crystal copper polygermanate ($CuGeO_3$) due to the isotypic nature of the compounds. The rest of the spectra were assigned in accordance with data provided by Spizzirri [38] whose experiments required a controlled micro-Raman analysis of a high quality thermally grown SiO_2 layer upon a Si substrate. They found a correlation between their control work and Si-O stretches and vibrations from silicate glass. The typical room temperature Raman spectrum (see **Fig. S5**, supporting information) was measured from 100-3200 cm^{-1} from a sample prepared at optimum conditions.

The spectrum can be separated into various regions of different slopes. The low frequency region is characterised by a dominant peak stationed at about 125 cm^{-1}. The high intensity of this peak, which originates from the Cu-Si vibrations, essentially signifies that it is in most abundance within the sample. The mid-spectral region depicts a definite spike at 520 cm^{-1} which corresponds to the first order Raman active phonon (TO) of silicon situated at the centre of the brillouin zone which arises as a result of the generation of the triply degenerate, long wave, transverse optical phonon. The final part of the spectrum under scrutiny is the broad expanse from 850-1700 cm^{-1} which is a combination of various Raman signals. The second order phonon which begins at ~850-1100 cm^{-1} arises from the second order Raman signal for silicon [39]. Then from 1200-1650 cm^{-1} there are a cluster of signals merged into one peak. The first component of the expanse is the peak at 1319 cm^{-1} which is thought to be attributed to the stretching mode of a bridging Cu-O-Si stretch. The broad expanse emerging at the end of the spectrum from ~1300-1650 cm^{-1} develops as a result of a combination of the third order optical phonon zone for silicon and also due to carbon impurity upon the surface of the sample. This region of the Raman spectrum is normally associated with the defect density and quality of carbon films [40]. The D (~1,350 cm^{-1}) and G (~1,600 cm^{-1}) peaks are related to structural disorder (sp^3 carbon) and order (sp^2 carbon), respectively and the relative intensities of these peaks (I_D/I_G) is useful for the comparison of the defect concentration across various samples. However, as was previously mentioned by Mukhopadhyay *et al* [41] in their thermodynamic thermal investigation of the MOCVD of copper films from Cu(tmhd)$_2$ found that carbon free copper is formed even in an inert argon atmosphere. Their findings showed that for relatively low temperatures (350 ºC) and pressures up to 1.6 kPa (12 torr), carbon present in the system will be reacted fully to create carbon monoxide, isobutene and acetaldehyde in the gaseous phase leaving Cu to be deposited in the solid phase. With this in mind it appears that the temperatures used in the formation of these nanostructures are too high to produce impure carbon-copper deposits. Also there is no indication upon the XRD spectrum to suggest that there is any carbon impurity within the region.

Similar results were obtained by Kono *et al.* [42] in their characterisation of mid ocean ridge basalt and an explanation afforded by Kanzaki [43] suggests that these

peaks are simply the result of carbon impurities and not from the first order scattering and Si-O stretching vibrations from highly coordinated Si in the local structure. As for starters, it has long been established that first order Si-O and IR bonds occur from 700-1200 cm^{-1}. Raman spectra of poorly crystallised graphite are known to contain broad signals at 1350 cm^{-1} and 1600 cm^{-1} and the intensity ratio of these two bands are commonly used to characterise carbon materials and therefore it is highly probable that these peaks in the spectrum are the result of carbon impurity. The source of carbon would most likely come from the decomposition of the $Cu(tmhd)_2$ precursor. The carbon containing materials would be made into poorly crystalline graphite during the high temperature growth process. However, the fact that no carbon was detected in either XRD or STEM insinuates that this is most likely just be adventitious carbon upon the sample surface.

STEM analysis

Focused ion beam lithography was performed upon samples of the selected individual nanostructures to localize sites of interest and create lamellae and a FEI Titan transmission electron microscope was used to characterise the lamella. STEM was carried out on the created lamellas and the internal structures of the nanostructures were then assessed using EDX to give us an insight into their composition and formation. The o-$Cu(SiO_3)$, w-$Cu(SiO_3)$ and w-Cu_3Si nanostructures were all analysed by STEM.

Fig. 6 displays a sectorial cross section of the o-$Cu(SiO_3)$ projected along the Si<110> directions. The o-$Cu(SiO_3)$ nanowire consists of a half an octahedron partially embedded (~200 nm) deep within the Si(100) substrate and a hemispherical cap entombed within a layer of SiO_2. The interfacial planes between the Si and $Cu(SiO_3)$ are at 55° to the substrate surface while the angle between these two interfaces converges at 62°. Internal lengths and widths of this structure were measured to be 523 nm and 387 nm respectively. Ribbons of Cu can be seen interwoven within the substrate below the o-$Cu(SiO_3)$ structure, highlighting that the deposition process is clearly accompanied by a large scale diffusion process both at and around the interface. Investigation of the internal composition reveals that the structure is largely composed of a polysilicate material. The base edges of the lower portion of the structure mainly consists of grey oxide material while the brighter beige bulk of the structure comprises of the Cu-Si intrusion with patches of the dark oxide being interwoven within the nanostructure.

The STEM cross section, from the Si<110> directions, of a w-$Cu(SiO_3)$ produced on the Si(100) substrate is shown in **Fig. S6** (supporting information). Unlike many of the w-$Cu(SiO_3)$ that were entrenched within the substrate, this sample was grown upon the surface at the Si/SiO_2 interface. The internal width reached a distance of 137 nm while the length measured 125 nm. The EDX analysis of the w-$Cu(SiO_3)$, again emphasised the polysilicate nature of the architecture containing various concentrations of Cu, Si and O. The thick black line just below the actual wire has been determined to be SiO_2. The image again draws attention to the diffusion of Cu into the subsurface via the ring positioned directly below the surfacial SiO_2 layer. The emergence of the Pt peaks reveals that the w-$Cu(SiO_3)$ was partially contaminated during the FIB process.

The w-Cu_3Si pictured below in **Fig. 7** outlines a sectorial shaped STEM image of a nanowire cross section, projected along the <110> growth directions. The

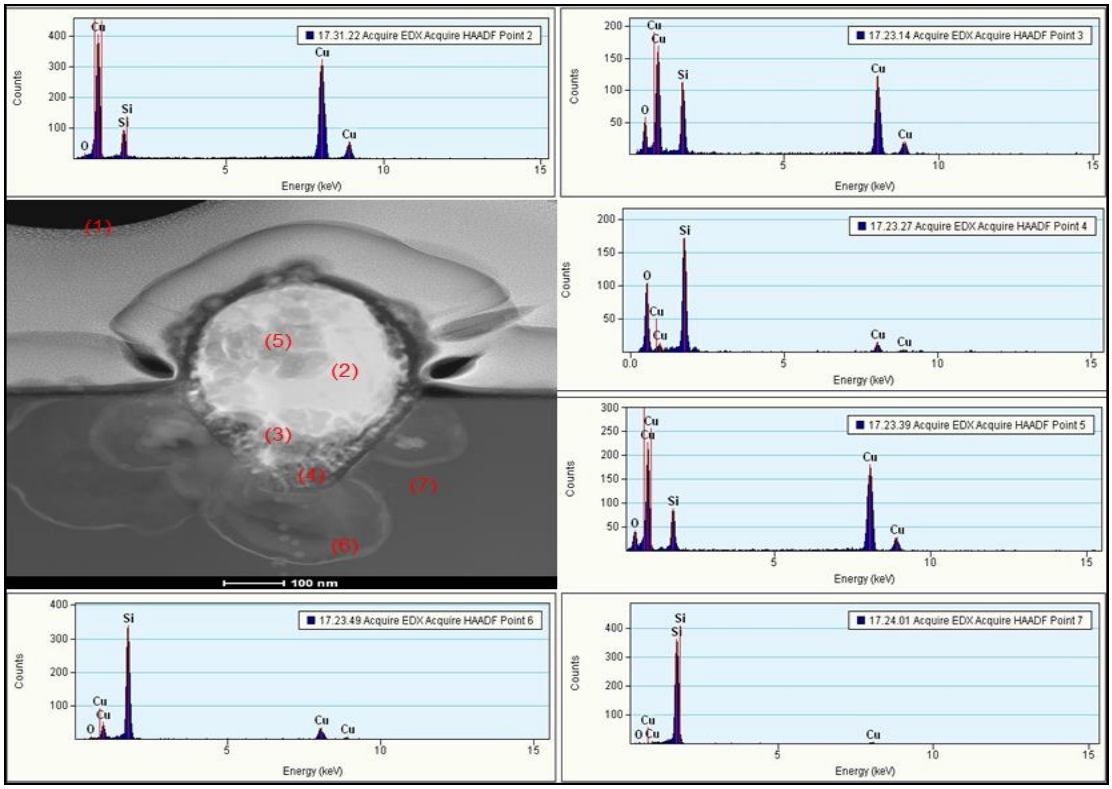

Fig. 6. STEM illustration of o-$Cu(SiO_3)$ and the associated EDX spectra at various regions of interest.

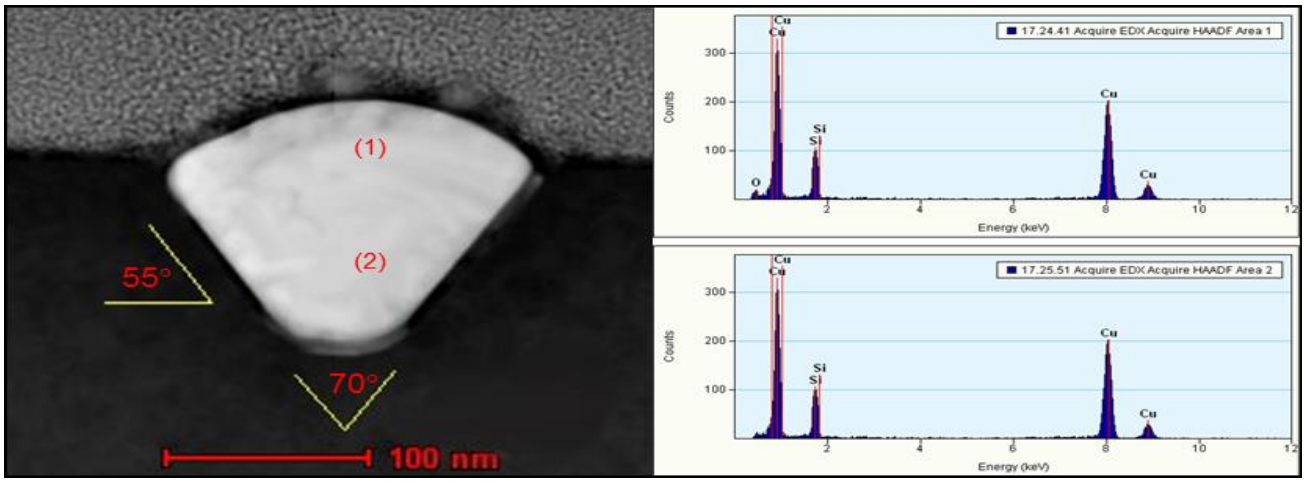

Fig. 7. STEM illustration of w-Cu_3Si and the associated EDX spectra at the various labelled regions of interest. A slight oxide intrusion is visible around the crown of the wire.

interfacial planes between the Si and the Cu_3Si wire is 55° to the surface of the substrate while the angle between the two interfaces is 70°. It is entrenched about 120 nm within the surface at the SiO_2/Si interface and it measures 145 nm at its widest point internally. It is known that the creation of Cu_3Si is associated with a required lattice expansion as approximately 1.3Si interstitial atoms are emitted for each Si atom forming a silicide [**43**]. Analysis of the wires chemical compositions via EDX indicated that the wire is comprised of 74% Cu and 26% Si which according to the Cu-Si phase diagram [**44**] makes it in keeping with the η-Cu_3Si phase. However, η-Cu_3Si is polymorphic, meaning that there are three stable Cu-Si phases that can be transformed at different temperatures. These phases are denoted by; η (which is stable above 600 °C), η' (which is stable above 531 °C) and η'' (which stable at room temperature and is the most common [**45**]). With this in mind, as the wires were grown at 700 °C, the initial structure is anticipated to be the η-Cu_3Si phase which slowly transforms through the η' phase and the η''- Cu_3Si phase upon cooling. The majority of the w-Cu_3Si was composed of a relatively uniform texture however it was noted that there were minute cracks of oxide visible at the crown of the wire that were determined to be derived from the post FIB ambient oxidation prior to loading it in the TEM. However, w-Cu_3Si was only the minor product of the deposition as according to XRD, Raman spectroscopy and other analysis above Cu(SiO_3) nanostructures were dominating due to the oxidation of initial w-Cu_3Si.

Discussion of Growth Mechanism

It has been previously proposed that oxidized metallic precipitates can be formed within silicon as a result of the different types of metal atoms, such as Cu and Fe, having a higher binding energy to the oxidized forms like oxides and silicates as opposed to silicides [**46**]. Metals and oxygen can form strong bonds, however an analysis of the competing oxidation power-play with silicon should be taken into account when trying to determine whether a species is a silicide, silicate or simply a metallic oxide should be formed [**47**]. It is common knowledge that silicon can accommodate interstitial oxygen [O_i] aggregates which are both stable and electrically inactive within the silicon matrix as well as harbor a native layer of SiO_2 upon its surface [**48**]. By comparing the enthalpies of formation per mole, per oxygen atom with a selection of elements for a variety of oxidized species, it can be deduced that equilibrium thermodynamics will largely favour silicon to be the principally oxidized species [**49**]. Cros *et al* demonstrated through a solid state reaction [**50**], that upon annealing an oxidized surface of Cu_3Si, the initially formed Cu_2O disappears and gives way to a much larger layer of SiO_2 due to the sizeable difference in the free energies of formation between Cu_2O and SiO_2. While on a much smaller scale, it has been calculated using first principles molecular dynamics simulations based on spin averaged and spin polarized density functional theory [**51**], that despite the attraction between interstitial copper Cu_i^+ and interstitial oxygen O_i, whose binding energy is quite small (0.31eV), no covalent Cu-O overlap takes place. The evidence provided as well as μ-XAF experiments that were carried out by Buonassisi and co-workers [**47**] would suggest that Cu in the presence of silicon with a low oxygen concentration will most likely, remain dissolved (solubility permitting), outdiffuse itself or become some form of unoxidised precipitate such as a silicide.

It has been noted that Czochralski (CZ-Si) silicon has a relatively high oxygen concentration in comparison to other types of silicon. Zundel *et al*. [**52**] initially discovered that the diffusivity of Cu in CZ-Si decreased as a result of a weak trap whose concentration matched that of an O_i. Transient-ion-drift experiments were run by Mesli *et al*. [**53**] between CZ-Si and float zone silicon that had been comparatively doped (p-type). It was found that the oxygen concentration in the CZ-Si sample was two orders of magnitude greater than that of float zone silicon and they managed to provide evidence [**54**] for a $^+$ pair with a 0.20 ±0.05 eV binding energy.

With this in mind and on the basis of the aforementioned results, we postulate there are several reactions occurring during the formation of these nanostructures. Upon injection, the $Cu(tmhd)_2$ is flash-evaporated into the gas phase and subsequently transported to the substrate in the deposition chamber by a constant

flow of inert argon gas where the Cu species are accommodated by both point defects such as nano-voids and interstitial oxygen precipitates and extended defects such as dislocations and stacking faults. From annealing blank samples of the Si(100) substrate under inert conditions at high temperatures, no voids were apparent from our studies and therefore it is believed that these voids are created as a result of SiO desorption from the substrate at high temperatures which is aided by the relatively high catalytic ability of Cu_3Si to oxidation which is in agreement with literature results. The o-Cu(SiO_3) form around defects in the substrates, dissolved oxygen precipitates mostly, via a void filling mechanism by copper, similar to that put forth by Li *et al* [**32**]. The voids are created due to the desorption of silicon oxide along the Si{111} planes as they have the highest atomic surface density and the reactions occur along this direction kinetically, as was shown by XRD. It is expected that after accommodation of the material in the voids, precipitation of the Cu_3Si occurs via the reactions:

$$3Cu + Si \rightarrow Cu_3Si$$

$$2CuO + Si \rightarrow 2Cu + SiO_2$$

After nucleation, the Cu_3Si/Cu(SiO_3) grow to fill the voids and undergo a series of shape and phase conversions to form nanosquares and nanoplatelets on the Si(100) substrate. Then in order to reduce the interfacial energy [**4**], these precipitates are then grown with a hemispherical cap provided that they are uninhibited by the template of the nanovoids (i.e. once they overgrow the template of the void). The reactions are diffusion limited as the silicon lattice is strained by the flux of copper through the material. Metal and metal oxide precipitation partially relaxes this strain at the SiO_2/Si interface where these precipitates become new sites for the nucleation of voids while also acting as a catalyst for the desorption of silicon dioxide [**32**]. W-Cu(SiO_3) is created from the surface diffusion of Cu at the surface of the substrate, while w-Cu_3Si is derived from a subsurface diffusion mechanism as can be seen from the STEM results. The generation of Cu_3Si is associated with a lattice strain at the nanowire tip region. Wire growth is catalysed by the quicker alignment and hardening of filled voids directed along the orientation of the substrate. Anisotropic growth occurs when the filled voids diffuse to the nanowire tips which are highly strained. We believe that spindle shaped nanostructures are initially formed by w-Cu_3Si which is then oxidised into w-Cu(SiO_3). Cu silicates can also occur via a more favourable kinetic pathway in the SiO_2 environment. The elongated reaction time/lengthening the time between the injections allows Cu which precipitates in the voids to reach their thermodynamically desired state of Cu_3Si. The reaction of Cu_3Si and Oxygen [**55**] can be described by the equation:

$$Cu_3Si + O_2 \rightarrow SiO_2 + 3Cu$$

The Cu atoms are liberated during the process and continue reacting via two routes. Provided that this reaction occurs at the buried interface, this series of events of can carry on by interacting with the substrate via $3Cu + Si \rightarrow Cu_3Si$ reaction, which is then followed by the oxidation of Cu_3Si at Si/SiO_2 interface.

Alternatively, copper atoms aggregate and form precipitates which are in turn oxidised by ambient oxygen upon cooling to copper oxide at this interface:

$$Cu + O_2 \rightarrow 2Cu_2O + O_2 \rightarrow 4CuO$$

In total these equations should result in the formation of $CuSiO_3$:

$$CuO + SiO_2 \rightarrow CuSiO_3$$

In addition as was stated earlier, it was shown by Cros *et al*. [**50**] that cuprous oxide was initially formed during the oxidation of Cu_3Si, which means that copper silicate should also appear in the reaction:

$$Cu_3Si + 2O_2 \rightarrow CuSiO_3 + Cu_2O$$

This can be clearly applied to our work to illustrate the abundance of Cu(SiO_3) that have been confirmed by XRD, Raman and STEM analysis.

Conclusion

In this work it was shown that various Cu(SiO_3) nanostructures can be grown at extended internal defects in Si(100) using the PI-MOCVD technique. An array of nanostructures, o-Cu(SiO_3), w-Cu(SiO_3) and w-Cu_3Si (embedded in silicate shell) were grown by utilizing a design of experiment like approach which allowed for the optimisation of the individual parameters, such as deposition temperature, reaction time, concentration and flow rate. The structures grown show a relative directional regularity in accordance with the orientation of the substrate. Both kinetic and thermodynamic effects were determined to play a significant role during the formation of the nanostructures. Depositions were diffusion limited and various techniques were used to show that by changing the amount of stress relaxation via the concentration and flow rate, w-Cu_3Si could be made to evolve. Low flow rates (50/50-100/100 ml/min) with low concentrations (n=50-100) were required for the creation of w-Cu_3Si upon Si(100). Characterisation of these structures by STEM showed that the subsurface wire structures were composed of the orthorhombic η‘‘-Cu_3Si while surface formed nanosquare and platelet structures were largely composed of the rhombohedral and orthorhombic phases of copper silicate and polysilicate respectively with varying amounts of silicon dioxide being ever present. Raman spectroscopy exhibited the presence of micro-defects were the cause of precipitation, more specifically, point defects such as nano-voids and disolved interstitial oxygen precipitates. It also revealed the presence of surface adventitious carbon. We believe that the presence of oxygen precipitates in the substrate allows for the kinetic formation of the metal oxide/silicate structures in spite of the fact that an analysis of the heats of formation of SiO_2 and Cu oxides would deem their generation thermodynamically unfavourable. The mechanism of formation of the structures is carried out through a void filling process in accordance with that purported by Li *et al.* It is also been thought that exposure of copper silicide to ambient oxygen at room temperature helped to contribute to the formation of copper silicate. This research puts foreward a potential for the fabrication of various patterned copper nanostructures using PI-

MOCVD. In overall, we expect this work to make a contribution to the further development of copper based nanostructures and their utilisation in a range of areas of science and technology especially in the field of copper interconnects in the integrated circuit technology.

Acknowledgements

The Authors would like to thank Dermot Daly for his help with the FIB. This work was supported by Science Foundation Ireland (Grant SFI 12/IA/1300).

Author's contributions

ROD prepared precursors. ROD and AT performed deposition experiments and characterisation of nanostructures by all instrumental techniques. YG contributed to experimental design. ROD and Yg wrote the manuscript.Authors have no competing financial interests.

Supporting information

Include all the supporting information data here like

(a) XRD patterns
(b) Selected SEM images
(c) AFM images
(d) Raman spectra
(e) Selected STEM results and EDX spectra.

References

1. Schmitt, A.L.; Higgins, J.M.; Szczech, J.R.; Jin, S. *J. Mater. Chem.* **2010**, *20*.223–235. **DOI:**10.1039/B910968D.
2. Ng, P.K.; Fisher, B.; Low, K.B.; Joshi-Imre, A.; Bode, M.; Lilley, C.M. *J. Appl. Phys. (Melville, NY, U. S.)* **2012**, *111*.104301. **DOI:**10.1063/1.4712536.
3. Hymes, S.; Kumar, K.S.; Murarka, S.P.; Ding, P.J.; Wang, W.; Lanford, W.A. *J. Appl. Phys. (Melville, NY, U. S.)* **1998**, *83*.4507–4512. **DOI:**10.1063/1.367235.
4. Seibt, M.; Griess, M.; Istratov, A.A.; Hedemann, H.; Sattler, A.; Schröter, W. *Phys. Status Solidi A* **1998**, *166*.171–182. **DOI:**10.1002/(SICI)1521-396X(199803)166:1<171:AID-PSSA171>3.0.CO;2-2.
5. Solberg, J. *Acta Crystallogr., Sect. A: Cryst. Phys., Diffr., Theor. Gen. Crystallogr.* **1978**, *34*.684–698. **DOI:** 10.1107/S0567739478001448.
6. Kajbaji, M.E.; Thibault, J. *Philos. Mag.* **1995**, *71*.335–339. **DOI:** 10.1080/09500839508241016.
7. Nes, E.; Lunde, G. *J. Appl. Phys. (Melville, NY, U. S.)* **1972**, *43*.1835–1837. **DOI:** 10.1063/1.1661405.
8. Stolt, L.; Charai, A.; d'Heurle, F.M.; Fryer, P.M.; Harper, J.M.E. *J. Vac. Sci. Technol., A* **1991**, *9*.1501–1505. **DOI:** 10.1116/1.577653.
9. Nes, E. *Acta Metall.* **1974**, *22*.81–87. **DOI:**10.1016/0001-6160(74)90127-8.
10. Nes, E.; Washburn, J. *J. Appl. Phys. (Melville, NY, U. S.)* **1971**, *42*.3562–3574. **DOI:**10.1063/1.1660771.
11. Istratov, A.A.; Hedemann, H.; Seibt, M.; Vyvenko, O.F.; Schröter, W.; Heiser, T.; Flink, C.; Hieslmair, H.; Weber, E.R. *J. Electrochem. Soc.* **1998**, *145*.3889–3898. **DOI**:10.1149/1.1838889.
12. Gottschalk, H. *Phys. Status Solidi A* **1993**, *137*.447–461. **DOI:**10.1002/pssa.2211370217.
13. Ludwig, G.W.; Woodbury, H.H. *Phys. Rev. Lett.* **1960**, *5*.98–100. **DOI:**10.1103/PhysRev.117.102.
14. Dash, W.C. *J. Appl. Phys. (Melville, NY, U. S.)* **1956**, *27*.1193–1195. **DOI**:10.1063/1.1722229.
15. Shen, B.; Sekiguchi, T.; Zhang, R.; Shi, Y.; Zheng, Y.D.; Sumino, K. *Phys. Status Solidi A* **1996**, *155*.321–332. **DOI:**10.1002/pssa.2211550205.
16. Maurice, J.; Colliex, C. *Appl. Phys. Lett.* **1989**, *55*.241–243. **DOI:**10.1063/1.101919.
17. Coteau, M.D. de; Wilshaw, P.R.; Falster, R. *Phys. Status Solidi A* **1990**, *117*.403–408. **DOI:**10.1002/pssa.2211170209.
18. Ryoo, K.; Drosd, R.; Wood, W. *J. Appl. Phys. (Melville, NY, U. S.)* **1988**, *63*.4440–4443. **DOI:**10.1063/1.340163.
19. Apátiga, L.M.; Rubio, E.; Rivera, E.; Castaño, V.M. *Surf. Coat. Technol.* **2006**, *201*.4136–4138. **DOI:**10.1016/j.surfcoat.2006.08.016.
20. Deschanvres, J.L.; Jimenez, C.; Rapenne, L.; McSporran, N.; Servet, B.; Durand, O.; Modreanu, M. *Thin Solid Films* **2008**, *516*.1461–1463. **DOI:**10.1016/j.tsf.2007.03.089.
21. Crepelliere, J.; Popa, P.L.; Bahlawane, N.; Leturcq, R.; Werner, F.; Siebentritt, S.; Lenoble, D. *J. Mater. Chem. C* **2016**, *4*.4278–4287. **DOI:**10.1039/C6TC00383D.
22. Hammond, G.S.; Nonhebel, D.C.; Wu, C.-H.S. *Inorg. Chem.* **1963**, *2*.73–76. **DOI:**10.1021/ic50005a021.
23. Zherikova, K.V.; Morozova, N.B.; Baidina, I.A.; Sysoev, S.V.; Igumenov, I.K. *J. Struct. Chem.* **2008**, *49*.58–63. **DOI:**10.1007/s10947-008-0009-4.
24. Zhang, S.; Wu, J.; He, Z.; Xie, J.; Lu, J.; Tu, R.; Zhang, L.; Shi, J. *AIP Adv.* **2016**, *6*.55106. **DOI:**10.1063/1.4948976.
25. Jung, S.J.; O'Kelly, C.J.; Boland, J.J. *Cryst. Growth Des.* **2015**, *15*.5355–5359. **DOI:**10.1021/acs.cgd.5b00947.
26. Jung, S.J.; Lutz, T.; Bell, A.P.; McCarthy, E.K.; Boland, J.J. *Cryst. Growth Des.* **2012**, *12*.3076–3081. **DOI:**10.1021/cg300273d.
27. Ermakov, K.; Ognev, A.V.; Samardak, A.; Kozlov, A.; Ovsaynnikov, A.; Mikoluk, E.; Chebotkevich, L.A.; Saranin, A.; Romashev, L.; Solin, N.*; et al. Solid State Phenom.* **2014**, *215*.204–207. **DOI:**10.4028/www.scientific.net/SSP.215.204.
28. Yuan, F.-W.; Wang, C.-Y.; Li, G.-A.; Chang, S.-H.; Chu, L.-W.; Chen, L.-J.; Tuan, H.-Y. *Nanoscale* **2013**, *5*.9875–9881. **DOI:**10.1039/C3NR03045H.
29. Chiu, C.-H.; Huang, C.-W.; Chen, J.-Y.; Huang, Y.-T.; Hu, J.-C.; Chen, L.-T.; Hsin, C.-L.; Wu, W.-W. *Nanoscale* **2013**, *5*.5086–5092. **DOI:**10.1039/c3nr33302g.
30. Geaney, H.; Dickinson, C.; O'Dwyer, C.; Mullane, E.; Singh, A.; Ryan, K.M. *Chem. Mater.* **2012**, *24*.4319–4325. **DOI:**10.1021/cm302066n.
31. Wen, C.-Y.; Reuter, M.C.; Tersoff, J.; Stach, E.A.; Ross, F.M. *Nano Lett.* **2010**, *10*.514–519. **DOI:**10.1021/nl903362y.
32. Li, S.; Cai, H.; Gan, C.L.; Guo, J.; Dong, Z.; Ma, J. *Cryst. Growth Des.* **2010**, *10*.2983–2989. **DOI:**10.1021/cg1000232.
33. Johnson, D.C.; Mosby, J.M.; Riha, S.C.; Prieto, A.L. *J. Mater. Chem.* **2010**, *20*.1993. **DOI:**10.1039/b919281f.
34. Zhang, Z.; Wong, L.M.; Ong, H.G.; Wang, X.J.; Wang, J.L.; Wang, S.J.; Chen, H.; Wu, T. *Nano Lett.* **2008**, *8*.3205–3210. **DOI:**10.1021/nl8015208.
35. Qi, J.; Masumoto, Y. *MRS Online Proc. Libr.* **2000**, *638* **DOI:**10.1557/PROC-638-F12.5.1.

36. Maruyama, T.; Ikuta, Y. *J. Mater. Sci.* **1993**, *28*.5540–5542. **DOI:**10.1007/BF00367827.
37. Meibohm, M.; Hermann, O.H.; Brockener, W. Vibrational spectra of copper polysilicate, $CuSiO_3$, **2009**, *1*. Available online: https://arxiv.org/ftp/arxiv/papers/0903/0903.3901.pdf.
38. Spizzirri, P.G. Probe enhanced, nano-Raman spectroscopy (PERS); A sensitive technique for vibrational surface spectroscopy. In Microscopy: Science, Technology, Applications and Education, 4th ed; Méndez-Vilas, A., Diaz, J., Eds.: FORMATEX: Spain, **2010**, pp. 1389–1396.
39. Katar, S.; Labiosa, A.; Plaud, A.E.; Mosquera-Vargas, E.; Fonseca, L.; Weiner, B.R.; Morell, G. *Nanoscale Res. Lett.* **2009**, *5*.74–80. **DOI:**10.1007/s11671-009-9446-z.
40. Havener, R.W.; Ju, S.-Y.; Brown, L.; Wang, Z.; Wojcik, M.; Ruiz-Vargas, C.S.; Park, J. *ACS Nano* **2012**, *6*, 373. **DOI:**10.1021/nn2037169
41. Mukhopadhyay, S.; Shalini, K.; Devi, A.; Shivashankar, S.A. *Bulletin of Materials Science* **2002**, *25*, 391. **DOI:**10.1007/BF02708016
42. Kono, Y.; Ohfuji, H.; Higo, Y.; Yamada, A.; Inoue, T.; Irifune, T.; Funakoshi, K.-i. *J. Mineral. Petrol. Sci.* **2008**, *103*, 126. **DOI:**10.2465/jmps.071022c.
43. Kanzaki, M. *J. Mineral. Petrol. Sci.* **2008**, *103*, 427. **DOI:**10.2465/jmps.080514
44. H. Okamoto. *J. Phase Equilib. Diffus.* **2012**, *33*, 415. **DOI:**10.1007/s11669-012-0076-2
45. Wen, C.-Y.; Spaepen, F. *Philos. Mag.* **2007**, *87*, 5581. **DOI:**10.1080/14786430701675829
46. McHugo, S.A.; Thompson, A.; Lamble, G.; Flink, C.; Weber, E. *Phys. B (Amsterdam, Neth.)* **1999**, *273*, 371. **DOI:**10.1016/S0921-4526(99)00480-9
47. Buonassisi, T.; Marcus, M.A.; Istratov, A.A.; Heuer, M.; Ciszek, T.F.; Lai, B.; Cai, Z.; Weber, E.R. *J. Appl. Phys. (Melville, NY, U. S.)* **2005**, *97*, 63503. **DOI:**10.1063/1.1827913
48. Ghita, R.; Logofatu, C.; Negrila, C.-C.; Ungureanu, F.; Cotirlan, C.; Manea, A.-S.; Lazarescu, M.-F.; Ghica, C. Study of SiO2/Si Interface by Surface Techniques. In Crystalline Silicon - Properties and Uses; Sukumar Basu, Ed.: InTech: Rijeka, **2011**, pp. 22.
49. Lide, D.R.; CRC press inc. CRC handbook of chemistry and physics a ready-reference book of chemical and physical data; CRC: Boca Raton, Ann Arbor, London [etc.], **2003**.
50. Cros, A.; Aboelfotoh, M.O.; Tu, K.N. *J. Appl. Phys. (Melville, NY, U. S.)* **1990**, *67*.3328. **DOI:**10.1063/1.345369
51. West, D.; Estreicher, S.K.; Knack, S.; Weber, J. *Phys. Rev. B* **2003**, *68*.35210. **DOI:**10.1103/PhysRevB.68.035210
52. Zundel, T.; Weber, J.; Benson, B.; Hahn, P.O.; Schnegg, A.; Prigge, H. *Appl. Phys. Lett.* **1988**, *53*.1426. **DOI:**10.1063/1.99962
53. Mesli; Heiser. *Phys. Rev. B: Condens. Matter Mater. Phys.* **1992**, *45*.11632. **DOI:**10.1103/PhysRevB.45.11632
54. Huang, Y.; Duan, X.; Cui, Y.; Lauhon, L.J.; Kim, K.H.; Lieber, C.M. *Science* **2001**, *294*.1313. **DOI:**10.1126/science.1066192
55. Huang, H.Y.; Chen, L.J. *J. Appl. Phys. (Melville, NY, U. S.)* **2000**, *88*.1412. **DOI:**10.1063/1.373832

